

Collisional effects on the electrostatic shock dynamics in thin-foil targets driven by an ultraintense short pulse laser

A Sundström¹, L Gremillet², E Siminos³ and I Pusztai¹

¹ Department of Physics, Chalmers University of Technology, 412 96 Göteborg, Sweden

² CEA, DAM, DIF, F-91297 Arpajon, France

³ Department of Physics, Gothenburg University, 412 96 Göteborg, Sweden

E-mail: andsunds@chalmers.se

Abstract. We numerically investigate the impact of Coulomb collisions on the ion dynamics in high- Z , solid density cesium hydride and copper targets, irradiated by high-intensity ($I \approx 2\text{--}5 \times 10^{20} \text{ Wcm}^{-2}$), femtosecond, circularly polarized laser pulses, using particle-in-cell simulations. Collisions significantly enhance electron heating, thereby strongly increasing the speed of a shock wave launched in the laser-plasma interaction. In the cesium hydride target, collisions between the two ion species heat the protons and the cesium ions to $\sim \text{keV}$ temperatures, however, in contrast to previous work [A.E. Turrell et al., 2015 *Nat. Commun.* **6** 8905], this process happens in the upstream only, due to a nearly total proton reflection. In the case of a copper target, the ion reflection can start as a self-amplifying process, bootstrapping itself. Afterwards, collisions between the reflected and upstream ions heat these two populations significantly. When increasing the pulse duration, the spatial and temporal detachment of the shock and the laser piston increases and the shock formation can be studied without direct interference from the laser. For a $2.5 \mu\text{m}$ thick copper target, the electrostatic shock has time to decay into a long-lived hydrodynamic-like shock, with no ion reflection.

1. Introduction

The use of lasers to accelerate ions is a field of intense research [1], with many demonstrated or envisioned applications, such as imaging of electromagnetic fields in plasmas [2, 3], creation of warm dense matter [4–6], production of intense neutron sources [7], material testing [8, 9], laboratory astrophysics [10], and ion-beam therapy [11, 12]. Among the few laser-based ion acceleration mechanisms considered so far, including the extensively studied, and particularly robust, target normal sheath acceleration (TNSA), collisionless shock acceleration (CSA) is of particular interest due to its potential to produce a relatively narrowly peaked ion energy spectrum [13–18]. Collisionless shocks also play a role in particle energization in astrophysical plasmas [19, 20].

As the shock front passes by, the plasma is rapidly compressed and directional kinetic energy is converted into thermal energy. This can take place either through collisional processes, such as in hydrodynamic shocks – relevant in, e.g., inertial fusion plasmas [21, 22] and relativistic laser-plasma experiments [23] – or collisionless mechanisms, involving longitudinal electrostatic fields generated by space charge effects from shock compression [14]. Collisionless shocks can also hinge upon self-generated magnetic fields, such as those resulting from the Weibel instability [24, 25], yet such shocks, of turbulent character, develop at Mach numbers much larger than those of the laminar electrostatic shocks that we shall address here [26]. In relativistic laser-plasma interactions, electrostatic shocks can arise either from the forward push exerted by the laser’s ponderomotive force (or “laser piston”) [14] in the radiation pressure acceleration (RPA) regime, or from electron pressure gradients in nonuniform plasmas [17]. While “collisionless shocks”, as the name suggests, are sustained through collective collisionless plasma processes, Coulomb collisions may play a role in their dynamics. Indeed, a finite collisionality, while affecting the shock, does not necessarily disrupt it [27].

Although the effect of collisions is often deemed negligible in high-intensity laser-plasma interactions, due to the high particle energies, it can become important when using solid or near-solid density targets, especially if they contain elements of high atomic numbers. In this paper, we consider two scenarios where collisions play an important role: one has basic science interest while the other is relevant for high energy density applications. We also present cases with parameters in between, to clarify how changes in laser and target parameters affect the ion dynamics, and in particular the properties of the resulting electrostatic shocks. In all cases, we will consider a circularly polarized femtosecond (10–60 fs) laser pulse.

The first case we consider is motivated by the work by Turrell, Sherlock & Rose [28] (hereafter referred to as TSR), where it was reported that inter-species collisions in a cesium hydride (CsH) target induce ultrafast collisional ion heating, and essentially affect the shock dynamics. We find drastically different results compared to what is reported by TSR, even though we study essentially the same physical setup. Importantly, we do not observe the occurrence of ultrafast ion heating downstream of the shock, as most of the protons are reflected, and as such, there is no appreciable inter-species friction in the downstream. This discrepancy is likely due to a different behavior, at the high densities considered, of the different collision algorithms employed by TSR and us.

The other case we address was first considered in a recent study of ours [29] investigating ionization and collisional electron heating effects in solid copper solid targets, relevant for warm-dense-matter generation. Here, we focus on the ion dynamics and examine the impact on the generated shock of the increased electron density in copper compared to CsH. We also assess the sensitivity of the ion dynamics to the laser parameters and target thickness.

When using circular laser polarization, collisions dominate the electron heating, which, in turn, results in the formation of a stronger electrostatic shock compared to

a purely collisionless simulation. In the copper scenarios, the evolution of the shock is studied, from the initial radiation pressure acceleration (RPA) and the transition into an electrostatic shock, through a gradual dissipation of its energy, to the shock's demise. In particular, the onset of shock ion-reflection is found to be self-amplifying. Collisional friction between the upstream and reflected ions heat the upstream ion population, which enhances the fraction of reflected ions.

2. Simulation study

In this paper, we investigate two different target materials, cesium hydride (CsH) and pure copper (Cu), both at their respective solid density. We perform one-dimensional (1D) particle-in-cell (PIC) simulations with the Smilei PIC code [30] (version 4.1), which has a collision module that has been benchmarked [31] in the high-density/low-temperature regimes relevant for this paper. In all cases, we use a circularly polarized (CP), $\lambda = 800$ nm wavelength laser with a Gaussian temporal profile. The simulation box consists of 51200 cells over a length of $20 \mu\text{m}$ (resolution $\Delta x = 0.39$ nm). The electrons were initialized at a temperature of $T_{e,0} = 1\text{--}10$ eV and the ions at a temperature of $0.1\text{--}1.0$ eV.

Both target materials contain a highly charged, Z^* , ion species, such that the effect of collisions is significant. This high collisionality turns out to be of crucial importance for the electron heating. Since CP is used, the target electrons are energized through inverse Bremsstrahlung, rather than from the strongly inhibited $j \times B$ [32] or vacuum heating [33,34] mechanisms. In our recent work [29], we showed that collisional electron heating produces well-thermalized electron populations with temperatures in the $\sim 1\text{--}10$ keV-range.

The use of the CsH target was inspired by the work by TSR [28]. As a target material, CsH could be of interest for laser acceleration of protons since it contains hydrogen volumetrically, like a plastic target. An advantage of this material over plastic, though, is the much higher ionization degree (Z^*) that can be reached, hence enhancing collisional effects. Although practically challenging, due to the high chemical reactivity of CsH and difficulties in the target fabrication, it would, in principle, be possible to use CsH in an experiment.

The CsH target is composed of an equal number mixture of protons and cesium ions. The charge state of the Cs ions is set to a fixed value of $Z^* = 27$, corresponding to full ionization of the three outermost shells. The resulting quasi-neutral electron density is $n_{e,0} = 250 n_c$, where $n_c = \epsilon_0 m_e \omega^2 / e^2 \approx 1.7 \times 10^{21} \text{ cm}^{-3}$ is the critical density (ϵ_0 is the vacuum permittivity, m_e is the electron mass, ω is the laser frequency and e is the elementary charge), corresponding to a collisionless skin depth of $l_s = 8.0$ nm which is well resolved. The target thickness is 300 nm, as in the simulations of TSR.

Copper, on the other hand, lacks the embedded protons, but it is, from a practical standpoint, much more readily available as a target material. Copper is also relatively highly charged, which means that a copper target would present a collisionality

comparable to the CsH target. The lack of embedded protons makes copper less suitable for ion acceleration, but its high collisionality could be beneficial for other applications, such as warm-dense-matter generation [29]. In the related simulations, the copper ions are initialized with three fully ionized shells ($Z^* = 27$) and at solid density (corresponding to $n_{e,0} = 1307 n_c$ and $l_s = 3.5$ nm).

With the copper targets, two different target thicknesses and two different laser parameters were considered. The thinner target is 300 nm thick, as in the CsH simulations, which has the advantage of quicker heating and homogenization compared to a thicker target. The thicker (2.5 μm) target, on the other hand, can be more suitable for warm-dense-matter applications: A high energy density will be maintained over a longer time since hydrodynamic expansion takes longer to reach the interior of a thicker target. We note that at the high densities and ionization degrees considered here, the useful lifetime of the target can also be affected by radiative (Bremsstrahlung) losses. We find, however, that for our parameters, the radiative cooling time is typically of several picoseconds, so that Bremsstrahlung losses should not greatly impact the plasma dynamics during the integration time (≤ 1 ps) of our simulations.

We considered two different sets of laser parameters: an amplitude of $a_0 = 15$ ($I \approx 5 \times 10^{20} \text{ Wcm}^{-2}$) and full-width-at-half-maximum (FWHM) duration of 10 fs, as well as $a_0 = 10$ ($I \approx 2 \times 10^{20} \text{ Wcm}^{-2}$) and a FWHM duration of 60 fs. The former is used with both the CsH and Cu thin targets, and the latter is used for both the thin and thick Cu targets.

For an accurate modeling of Coulomb collisions, employing the relativistic PIC algorithm of [31], a relatively high number of particles per cell is needed. In the thinner target, 500 macro-particles per species per cell was used, while in the thicker target, the particle number was reduced somewhat to 400 macro-particles per species per cell. Resolution tests, with halved particle number or halved spatial resolution (with same total number of particles), for the Cu thin target simulation show that the simulations are numerically converged.

3. Ion dynamics in CsH target

Motivated by the previous work by TSR, we performed a similar set of simulations in CsH. However, despite virtually identical setups, our results differ significantly from the ones by TSR.

3.1. Comparison of collisional and collisionless results

The primary effect of the strong target collisionality is to significantly enhance electron heating through inverse Bremsstrahlung [29]. As an illustration of the collisional electron heating, Fig. 1 shows the electron phase space of the collisional (top row) and collisionless (bottom row) CsH simulations at three successive times: during peak laser intensity at $t = 21$ fs, right after the laser pulse has ended at $t = 45$ fs, and even later at $t = 70$ fs.

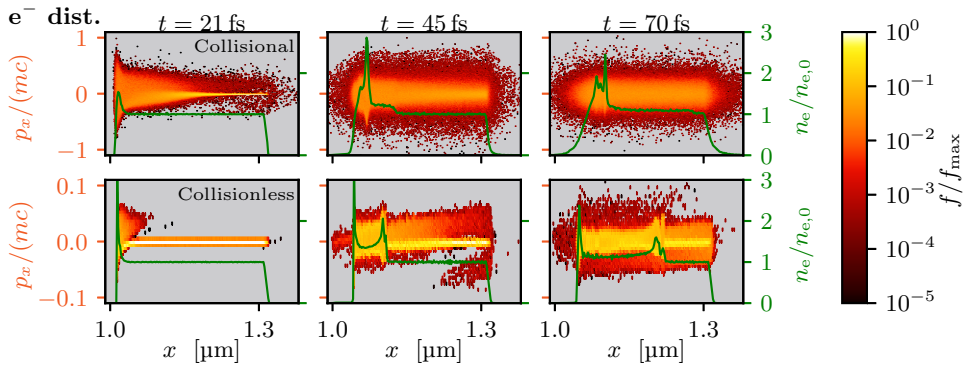


Figure 1. Electron distributions at (left) and after the laser peak intensity (middle and right), with (top) and without (bottom) collisions, using CP. Green curve: electron density. Please note the different momentum scales for the collisional and collisionless simulations.

In figures hereafter, the phase space distribution functions f are normalized to the maximum value of each respective *initial* Maxwellian distribution, f_{max} .

The electrons in the target front layer are energized in the transverse (y - z) plane by the laser electric field. Then collisions scatter their momentum into the longitudinal direction, as seen through the large spread in p_x near the plasma front in the $t = 21$ fs frame of the collisional distribution. Collisions then entail a fast thermalization of the electrons to a Maxwellian distribution, yielding a bulk temperature of $T_e \approx 10$ keV that corresponds to an ion-acoustic speed of $c_s \approx (Z_{\text{Cs}}^* T_e / m_{\text{Cs}})^{1/2} \approx 1.5 \times 10^{-3} c$.

The electron density is also indicated in Fig. 1 (green solid curve, right axis). Compared to the collisionless case, the collisional simulation shows smoother spatial structures likely due to a combination of higher temperature, collisional dissipation and dispersion of non-linear waves. The Debye length is $\lambda_D \approx 1$ nm and $\lambda_D \approx 0.1$ nm in the collisional and collisionless cases, respectively. The collisional electron density profile also shows signs of an electrostatic shock wave: a density jump moving away from the target front is visible in the $t = 45$ fs and 70 fs panels. In the collisionless case, the density profile exhibits two peaks in both time frames. The rightmost density jump is due to the leading edge of the radiation-pressure-accelerated Cs ions (Fig. 2), while the leftmost density peak corresponds to an electrostatic shock, which, due to the low electron temperature, is too slow for its propagation to be noticeable over the displayed time and length scales.

In Fig. 2, the evolution of the ion distributions in the collisional and collisionless CsH targets are shown. The top frame shows the proton, the lower one the Cs ion phase spaces, with the upper (lower) rows in both frames corresponding to the collisional (collisionless) simulations, at times $t = 21$ fs, $t = 45$ fs and $t = 70$ fs. At $t = 21$ fs, the difference between the collisional and collisionless simulations is quite small; in both cases, the protons and Cs ions are pushed by the laser piston. However, due to the lower charge-to-mass ratio of the Cs ions compared to the protons, the Cs ions react more

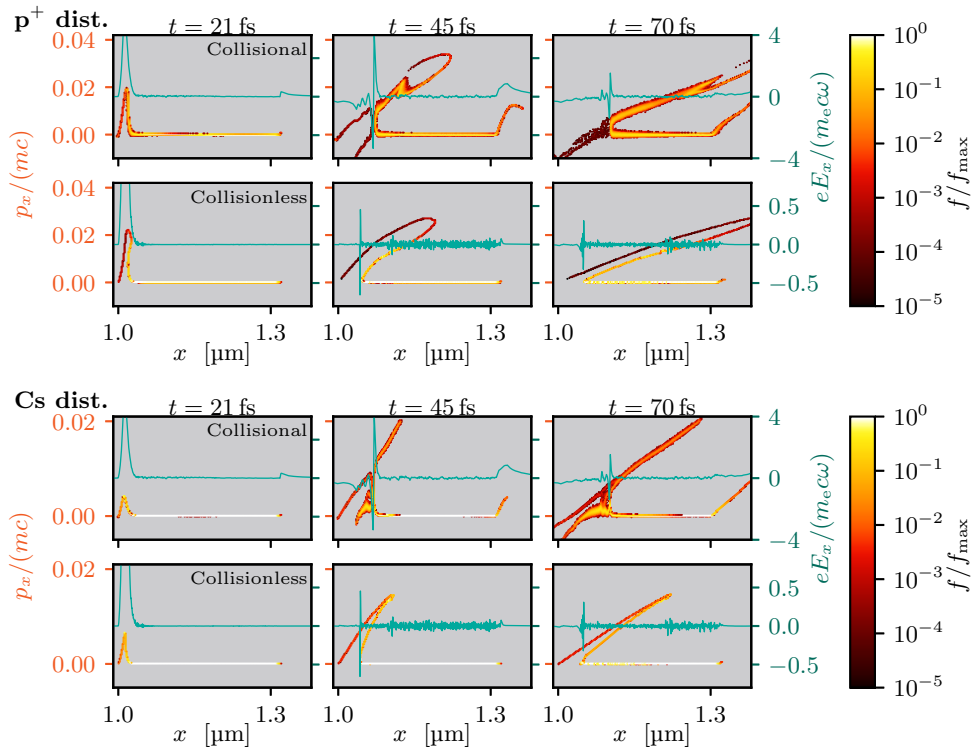


Figure 2. Proton (top frame) and cesium ion (bottom frame) distributions in the 300 nm CsH target at peak laser intensity ($t = 21$ fs) and after the pulse has passed ($t = 45$ fs and 70 fs), with (upper panels) and without (lower panels) collisions, using CP. The longitudinal electric field is also plotted (turquoise solid line, right axes). Note the different electric field scales between the collisional and collisionless panels.

slowly to the radiation pressure (RP) induced field (at $x \approx 1 \mu\text{m}$) than the protons, as seen by the almost four times higher velocity reached by the protons ($p_x/mc \approx 0.02$) at $t = 21$ fs. Owing to the short pulse duration (10 fs), the Cs ions do not have enough time to react to RP before the pulse ends.

Also shown in Fig. 2 is the longitudinal electric field, E_x (turquoise curve), normalized to $m_e c \omega / e \approx 4.013 \times 10^{12}$ V/m. The charge separation during the RPA phase creates a strong longitudinal electric field, visible as a positive spike in E_x close to $x = 1 \mu\text{m}$ in the $t = 21$ fs panels. Note that the peaks of the RPA field are cut off in the display. The collisionless RPA field reaches a normalized amplitude of 8.6, while the field in the collisional simulation reaches only 5.6. However, the RPA field in the collisional simulation has a wider spatial extent. When the electric field is integrated, the potential drop across the RPA field is $e\phi \approx 220$ keV and 280 keV in the collisionless and collisional cases, respectively. Thus, collisions do not affect the RPA process significantly, as apparent from the comparison of the collisional and collisionless panels at $t = 21$ fs in Fig. 2.

With collisions, the electrostatic structure caused by RPA transforms into an electrostatic shock, as evidenced by the single strong oscillation of E_x and modulation of the downstream ion distributions in the $t = 45$ fs and 70 fs frames of Fig. 2. A close

inspection of the collisionless simulation reveals oscillations in E_x and modulations of the downstream Cs ions (although barely visible at the scale in Fig. 2), which therefore indicates that a shock has been formed in the collisionless simulation as well. However, due to the high electron temperature from collisional heating, the shock is much stronger and faster in the collisional case. In absolute units, the average shock velocity between $t = 45$ fs and 70 fs were $v_{\text{sh}}/c \approx 4.3 \times 10^{-3}$ and $v_{\text{sh}}/c \approx 0.9 \times 10^{-3}$ in the collisional and collisionless simulations, respectively. Yet, the higher electron temperature in the collisional target ($T_e \approx 10$ keV vs. $T_e \approx 0.2$ keV) leads to a lower Mach number ($\mathcal{M} \approx 2.9$ vs. $\mathcal{M} \approx 4$). The low shock speed in the collisionless simulation implies that the shock-reflected ions have a significantly lower energy compared to those originating from the initial burst of the RPA. In both the collisional and collisionless cases, given its limited energy reservoir provided by the ultrashort (10 fs) laser pulse, the shock wave steadily loses its energy, as seen by the declining field amplitude and the sloped reflected ion structure in the proton and Cs phase spaces (i.e. the shocks are losing speed).

Another consequence of the efficient inverse Bremsstrahlung electron heating is that the collisional simulation displays TNSA at the target rear boundary, whereas it is virtually nonexistent in the collisionless simulation, as evident at $t = 70$ fs in Fig. 2. Due to the use of CP, the electrons are weakly energized in the collisionless case, hence quenching TNSA. In the collisional simulation, the TNSA protons attain energies slightly lower than the RPA protons at the final simulation time.

In the collisional case, we also see that the reflected and upstream proton and Cs ion populations are being significantly heated, in contrast to their collisionless counterparts. By fitting Maxwellians to the proton distribution in the range $x = 1.15\text{--}1.18$ μm (close to, but still beyond direct influence from the shock front) at time $t = 70$ fs, the upstream proton population is found to have already been heated to $T_p^{(i)} = 120$ eV, while the reflected protons are at a temperature of $T_p^{(r)} = 750$ eV. We recall that the initial ion temperature was 0.1 eV. Simulations in which various types of collisions (e.g., proton–Cs or ion–electron) have been selectively switched off (not shown here), reveal that the heating of the reflected ions is driven by collisional friction between the protons and Cs ions, while the heating of the upstream ions is mainly driven by their collisional thermalization with the hot electrons.

To get a more detailed picture of the vicinity of the electrostatic shock front, close-ups of the proton (top) and Cs (bottom) distributions, at $t = 70$ fs, are displayed in Fig. 3. The distributions have been shifted to the shock rest frame (at velocity $v_{\text{sh}}/c \approx 3.1 \times 10^{-3}$), relative to the position of the potential maximum, x_{sh} ; the velocities are normalized to the ion-acoustic sound speed, c_s . The electrostatic potential, $\phi(x) = -\int_{x_0}^x E_x(x') dx'$, where x_0 is such that ϕ averages to zero in the range $8 \leq (x - x_{\text{sh}})/\lambda_D \leq 10$, is also plotted (blue line), along with corresponding constant energy contours (black dashed or dotted lines). The black dashed line represents the constant energy contour which has zero (shock-frame) kinetic energy at the peak of ϕ . This line is an approximate boundary between the reflected and passing ions; in a steady state, this would be a separatrix. We clearly see that close to 100% of the protons (top

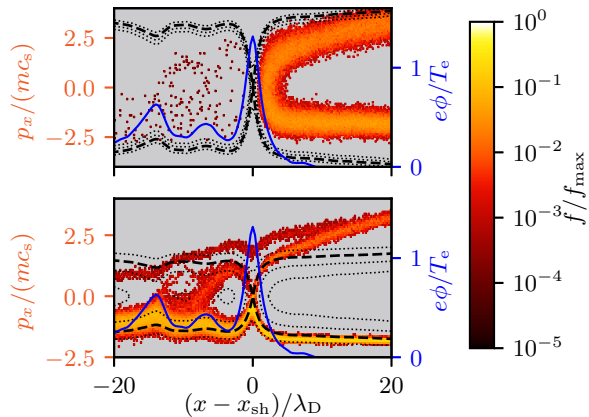


Figure 3. Proton (top panel) and Cs ion (bottom panel) distributions in the shock frame of reference at $t = 70$ fs, together with the shock electrostatic potential, $e\phi/T_e$ (blue solid line, right axes), using $T_e = 10$ keV. Also shown are contours of constant energy, $\mathcal{E} = mv^2/2 + eZ(\phi - \phi_{\max})$ (black, dashed or dotted lines). The black dashed line corresponds to $\mathcal{E} = 0$ at the potential peak, ϕ_{\max} .

frame) are within the reflected region of phase space. Meanwhile, only around 5–10% of the Cs ions are reflected, and accordingly, the upstream Cs distribution mostly lies below the passing–reflected boundary. The difference in ion reflection between the two ion species is due to their different charge-to-mass ratios [35].

The electrostatic potential is seen to oscillate downstream of the shock (left side in Fig. 3), which creates regions of ion trapping. In a perfectly steady-state and collisionless electrostatic shock, these regions would be empty, as there would be no means for the ions to cross the separatrix. However, due to adiabatic effects, caused by the decreasing amplitude and speed of the shock, the trapping regions experience a steady influx of Cs ions. These effects are likely more important here than collisional scattering [27]. While the Cs ions mainly enter the trapping regions from the leftmost potential hump in Fig. 3, almost no protons pass the shock front and hence only few protons ever enter the trapped region. The protons trapped in those regions are mostly remnants of the protons left behind the main RPA (seen to the left of the shock front in the $t = 45$ fs frame of Fig. 2).

3.2. Ultrafast ion heating revisited

The paper by TSR [28] reports on an *ultrafast collisional ion heating* phenomenon, appearing in multi-species plasmas with high- Z components. The process is born out of collisional 1D simulations with the EPOCH [36] PIC code, considering a CsH target identical to that in the current paper. The mechanism of the ultrafast ion heating is collisional friction between the protons and Cs ions as they experience a differential acceleration by the electrostatic shock field.

The CsH setup presented in this paper is almost identical[‡] to that of TSR – apart from a 1% difference in the electron density, the laser polarization and the increased resolution in our case. However, our results differ significantly. TSR observe the ion heating in the shock *downstream* as a result of collisional friction between the protons and the cesium ions, along with a complete absence of ion reflection. In our simulations, however, the collisional interaction between the two ion species is not sufficiently strong to extinguish the reflection of protons; in fact, as shown in e.g. Fig. 3, nearly all protons are reflected, and these are subsequently heated through collisional friction with the ambient (upstream) Cs ions. The ion heating is strongest in the *reflected* ion population.

TSR also offers an analytical model that appears to support their PIC results. It is a two-fluid model retaining the momentum and energy moments of the Boltzmann equation, assuming Maxwellian distributions. It provides steady-state expressions for the longitudinal derivatives of the temperatures and velocities of the two fluid species, which are then integrated over a distance corresponding to the width of the electrostatic shock front. The energy input to the system comes from an electric field term representing the electrostatic shock field. Importantly, it is assumed that there is no ion reflection and that all protons pass through the barrier, which is true in the context of their simulation results, but not in ours. In the collisionless case the protons should clearly be reflected due to their higher charge to mass ratio than that of Cs. The only way to avoid proton reflection is if a very strong friction between the two species pulls the ions across the potential barrier. This, however, requires a much stronger collisional coupling than what we observe.

Thus, we believe that the difference between the TSR and our results is a consequence of the different collision algorithms used. EPOCH [36], which was used by TSR, only had a collision module based on the algorithm by Sentoku & Kemp [37] (SK)[§], while Smilei’s [30] employs the algorithm proposed by Pérez et al. [31] (NYP), which generalizes to the relativistic regime the Nanbu & Yonemura scheme [38,39]. Both the SK and NYP algorithms include (distinct) corrections at low temperatures/high densities, where the standard small-angle scattering assumption breaks down. Yet a recent simulation study [40] of dense ($n_e = 60n_c$) plasmas driven at relativistic laser intensities did show that the two algorithms indeed produce qualitatively different results. Since the NYP algorithm was shown to reproduce the thermal variations in the electrical resistivity of dense plasmas as predicted by atomic physics models [31], we tend to believe that our simulation results for CsH are more realistic than those presented by TSR [28].

[‡] We have also performed a Smilei simulation with exactly the same physical parameters and numerical resolution as TSR. In terms of the ion dynamics, the results of that simulation are virtually the same as the CsH simulation presented in this paper, i.e. Fig 2.

[§] More recently (since version 4.17, released in June 2019) EPOCH now has the full NYP algorithm implemented, so that users now can select which algorithm to use.

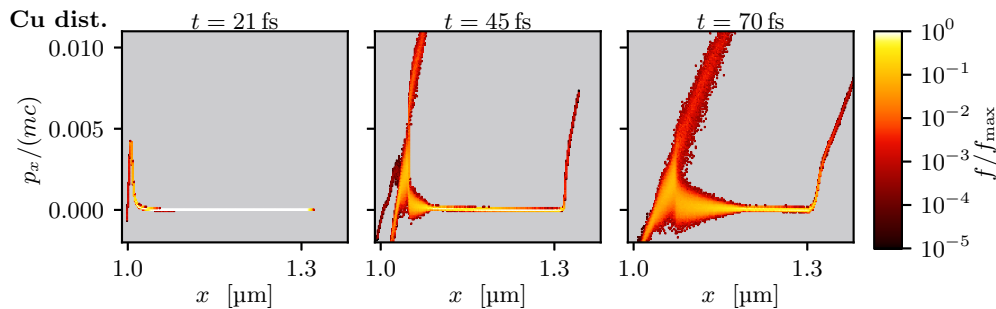


Figure 4. Copper ion phase-space distribution in the 300 nm Cu target from the collisional simulation, at times $t = 21$ fs, $t = 45$ fs and 70 fs.

4. Ion dynamics in copper targets

We will now turn to the pure copper simulations, first considering similar target and laser parameters to the CsH case, and subsequently changing these parameters one by one. The two main differences compared to CsH are the lack of multi-species effects and the ~ 5 times higher electron density (assuming $Z^* = 27$). However, just as in the CsH target, the primary effect of collisions in the Cu plasma is the collisional electron heating. The bulk electrons are heated to $T_e \approx 3.7$ keV, corresponding to a sound speed of $c_s \approx 1.3 \times 10^{-3} c$.

Figure 4 shows the collisional Cu ion phase-space distribution, at peak laser intensity ($t = 21$ fs), close after the laser irradiation ($t = 45$ fs), and even later in time ($t = 70$ fs). Similarly to Cs, the Cu ions have a rather low charge-to-mass ratio ($Z^*/A = 0.42$) and do not have time to fully respond to the laser piston during the short-pulse irradiation. Again, the initial perturbation from the laser piston transforms into an electrostatic shock. However, the shock is losing energy faster than their counterparts in the CsH target.

Since the copper plasma does not contain any protons, all of the reflected charge, needed to sustain the shock, consists of Cu ions. Owing to their high charge ($Z^* = 27$), the collisional interaction between the reflected and the upstream ions is stronger than in the collisional CsH case, resulting in a noticeable heating of these two populations, as seen in the collisional Cu ion distributions at 45 fs and 70 fs in Fig. 4. Some heating is observed in the collisional proton and Cs ion distributions of Fig. 2 as well, but significantly weaker than in the copper plasma.

We have also studied a scenario wherein the copper plasma is illuminated by a laser pulse of longer duration (60 fs FWHM) and lower intensity ($a_0 = 10$). The copper ion phase-space distribution from the collisional simulation is displayed in Fig. 5, shown at times $t = 90$ fs (at peak laser intensity), $t = 150$ fs (close to the end of the pulse) and $t = 200$ fs. Like in the two previous setups, an electrostatic shock forms. However, it is formed out of a shock-like perturbation, which propagates into the target faster than the laser piston. This pre-shock detaches from the laser piston already as early as $t \approx 60$ fs, before the pulse has reached half its maximum intensity. It displays shock-like

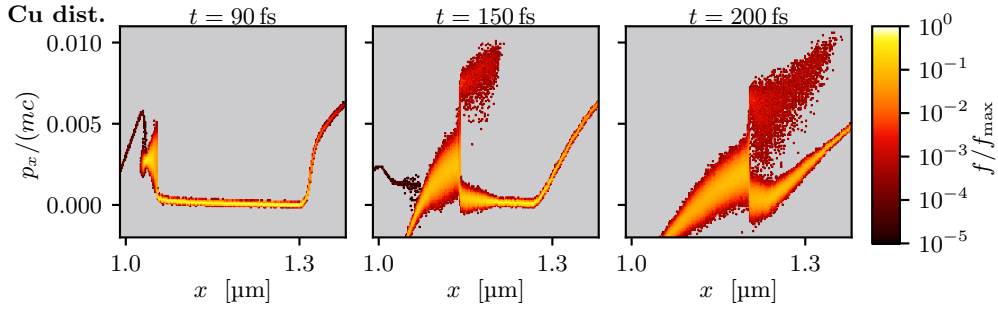


Figure 5. Copper ion phase-space distribution in the 300 nm Cu target from the collisional simulation, with an $a_0 = 10$ and 60 fs duration laser pulse. The distribution is shown at times $t = 90$ fs, $t = 150$ fs and 200 fs.

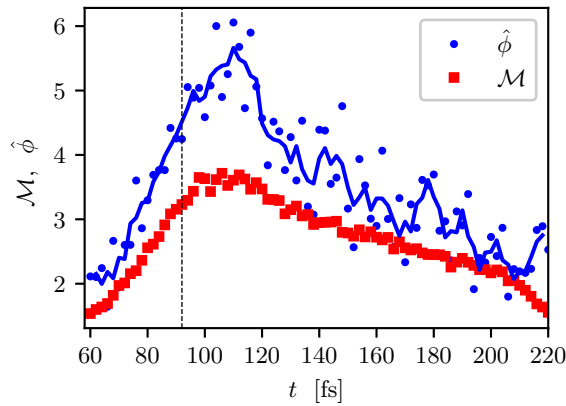


Figure 6. Temporal evolution of the normalized potential drop across the shock front, $\hat{\phi} = e\phi/T_e$, and shock Mach number, \mathcal{M} , for the thin copper target, long pulse collisional simulation. The blue line represents a moving average (over three data points) of $\hat{\phi}$. The thin vertical line denote the time of onset of ion reflection. For both the normalization of the potential and for the ion acoustic sound speed, an electron temperature of $T_e = 4$ keV was used as a representative value.

characters, such as a sharp rise in lab-frame ion velocity in conjunction with a step electrostatic potential barrier, but it lacks any ion reflection, as seen in the $t = 90$ fs frame of the collisional simulation.

Figure 6 shows the evolution of the normalized|| potential jump $\hat{\phi} = e\phi/T_e$ and Mach number \mathcal{M} of the shock from the time of detachment from the laser piston to its demise. The transition to a fully developed, ion-reflecting, electrostatic shock occurs when $\hat{\phi} \gtrsim \mathcal{M}^2/2$, which is at around $t \sim 90$ fs. The observed time of first ion reflection is at $t \approx 92$ fs. The longer pulse duration and more gradual increase in intensity, detaches the onset of shock reflection from RPA.

The peaks in $\hat{\phi}$ and \mathcal{M} are followed by a more gradual decrease in the Mach number

|| Using a fixed value of $T_e = 4$ keV, derived from Maxwellian fits to the electron energy spectrum (whole plasma). The measured electron temperature stays fairly close to this value during the entire duration of the pre-shock and the electrostatic shock.

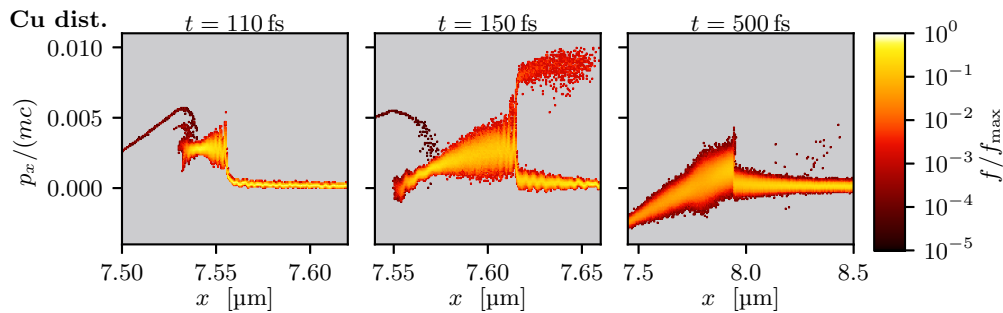


Figure 7. Distribution of copper ions in a 2.5 μm thick target, with collisions, at times $t = 200$ fs, $t = 400$ fs and 1000 fs.

and in the shock potential peak, starting at around $t \approx 110$ fs. The vertical lines in Fig. 6 represent the time of peak (solid) and half (dotted) laser intensity. The peaks thus occur before the laser intensity has halved. The reason for the delayed peaks in shock speed and potential relative to the peak laser intensity is likely related to a point, at which the laser is no longer able to supply more power than the energy dissipation rate of the shock.

The reflection of ions appears as a process bootstrapping itself. After the first few ions have been reflected, collisional heating between the upstream and reflected ions cause a broadening of the upstream ion longitudinal momentum distribution, leading to more ions entering the reflected region of phase-space. This upstream heating is seen in the collisional $t = 150$ fs frame of Fig. 5. Towards the end of the simulation, the upstream and reflected ion populations start to merge into each other, after which the determination of the shock speed relative to the upstream population becomes unreliable. The shock is somewhat abruptly ended when it collides with the rarefaction wave emanating from the back of the target, which occurs at roughly $t \approx 250$ fs.

As a final setup, we switch to a 2.5 μm copper target, driven by an $a_0 = 10$ and 60 fs FWHM duration pulse. Those parameters may be of interest to warm-dense-matter studies [29]. The simulation results are shown in Fig. 7. Despite the significant increase in target volume, the measured electron temperature still reaches $T_e \approx 3.5$ keV, thus the initial evolution of the shock is very similar to the corresponding thin-target simulation. Indeed, the Mach number and shock potential evolve similarly to those displayed in Fig. 6, both qualitatively and quantitatively (when accounting for a time shift of ≈ 15 fs corresponding to the different target position).

However, as the target is now significantly thicker, the shockwave has time to further dissipate its energy and the ion reflection stops well before the shock front encounters the rarefaction wave from the back of the target. As the shock steadily loses speed – and the electrostatic potential drop decreases – a point is reached when the field strength is not sufficient anymore to continue driving the ion reflection. We see in the $t = 500$ fs panel of the collisional simulation in Fig. 7, that there is still a sharp phase-space structure propagating inward, but there is no accompanying ion reflection. Apparently, the electrostatic shock has transformed into a more hydrodynamic-like shock structure,

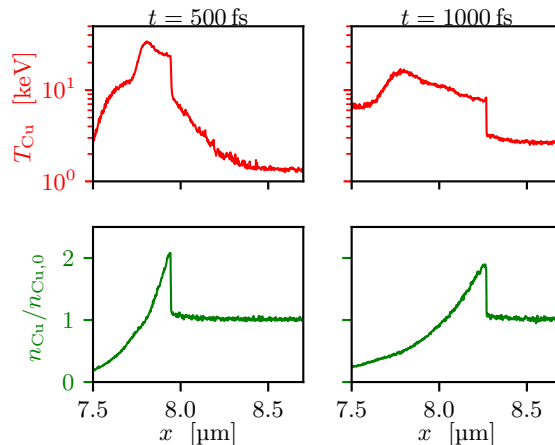


Figure 8. Spatial profiles of the copper ion temperature and density at $t = 500$ fs and $t = 1000$ fs. Both profiles display a sharp jump; the temperature jump by about a factor of 2.6, while the density jumps by about a factor 2.0. The sizes of these jumps remain essentially constant over the time interval displayed.

supported by collisional processes. This transition occurs at around $t \approx 300$ fs; at this time, the Mach number has dropped to $\mathcal{M} \approx 1.3$ and the shock electric field is within the numerical noise level.

Although there is no ion reflection occurring anymore, there are still clear signs of a shock-like structure in the ion temperature, T_{Cu} , and density, n_{Cu} , profiles. Figure 8 shows that T_{Cu} and n_{Cu} jump by a factor of 2.6 and 2.0, respectively, which remains essentially unchanged from $t = 500$ fs to $t = 1000$ fs. This time interval is significantly larger than the time scale for the loss of energy in the electrostatic shock. In the case of the temperature the absolute values decrease with time, while the relative size of the jump remains unchanged.

To investigate possible multidimensional effects on the laser-driven electron energization and subsequent ion dynamics, we have performed a two-dimensional simulation of the thick copper target, detailed further in [29]. This simulation reveals that the situation studied here is sufficiently collisional that the shock does not suffer from transverse modulations.

5. Conclusions

Using particle-in-cell simulations, we have numerically investigated the impact of Coulomb collisions on the ion dynamics in high- Z^* , solid density cesium hydride and copper targets, irradiated by high-intensity ($I \approx 2\text{--}5 \times 10^{20} \text{ Wcm}^{-2}$), femtosecond, circularly polarized laser pulses.

In all cases collisional absorption through inverse Bremsstrahlung heats the electrons up to 3–10 keV temperatures throughout the target, while the use of CP reduces the creation of high-energy electrons. Subsequently, collisions quickly relax

the electrons to a Maxwellian distribution. The impact of the laser pulse launches an electrostatic shock wave. In all cases studied here, the collisionally enhanced electron heating results in faster shock waves, with higher potential drops across the shock front, than in the corresponding collisionless simulations.

In the CsH target, the different charge-to-mass ratios of the hydrogen and cesium ions results in a strongly preferential reflection of protons. In contrast to the results of TSR [28], we do not observe the collisional friction between these species to cause a significant fraction of the protons to pass through the shock front. Instead, inter-species friction results in the *reflected* ions being heated up to \sim keV temperatures.

In pure Cu targets, the collisional coupling between the reflected and upstream ions is stronger, causing an appreciable heating of these two. Also, the higher density, of both ions and electrons, causes the shock to lose its energy more rapidly than in the CsH target. When changing the laser parameters to a somewhat lower-intensity, but longer-duration laser pulse, the initial stages of the shock launching process become more decoupled from the laser pulse and the RPA. Here, the shock forms already prior to the on-target laser peak. However, the shock front continues to accelerate until about \sim 20 fs after the peak on-target laser intensity. Because of the quick launch of the electrostatic shock, the maximum energy of the accelerated ions were more uniform, since there is no transition from RPA ion to CSA ions. However, the shock initially lacks ion reflection, the onset of which appears to be bootstrapping itself through the reflected-upstream ion heating.

Lastly, we increased the target thickness in order to follow the electrostatic shock evolution over a longer duration, and to become more relevant to high energy density applications. In this case, the shock speed and potential decay until the shock loses its capability to reflect ions. At this stage, the electrostatic potential drop across the shock front has also disappeared. However, a long-lived hydrodynamic-like shock structure remains, still propagating at supersonic speeds.

Acknowledgments

The authors are grateful for fruitful discussions with L. Hesslow and T. Fülöp, as well as to M. Grech and F. Pérez for support with Smilei. This project has received funding from the European Research Council (ERC) under the European Union's Horizon 2020 research and innovation programme under grant agreement No 647121, the Swedish Research Council (grant no. 2016-05012), and the Knut och Alice Wallenberg Foundation. The simulations were performed on resources provided by the Swedish National Infrastructure for Computing (SNIC) at Chalmers Centre for Computational Science and Engineering (C³SE) and High Performance Computing Center North (HPC²N).

References

- [1] Macchi A, Borghesi M and Passoni M 2013 *Rev. Mod. Phys.* **85**(2) 751–793
- [2] Borghesi M, Campbell D H, Schiavi A, Haines M G, Willi O, MacKinnon A J, Patel P, Gizzi L A, Galimberti M, Clarke R J, Pegoraro F, Ruhl H and Bulanov S 2002 *Physics of Plasmas* **9** 2214–2220
- [3] Romagnani L, Fuchs J, Borghesi M, Antici P, Audebert P, Ceccherini F, Cowan T, Grismayer T, Kar S, Macchi A, Mora P, Pretzler G, Schiavi A, Toncian T and Willi O 2005 *Phys. Rev. Lett.* **95**(19) 195001
- [4] Patel P K, Mackinnon A J, Key M H, Cowan T E, Foord M E, Allen M, Price D F, Ruhl H, Springer P T and Stephens R 2003 *Phys. Rev. Lett.* **91**(12) 125004
- [5] Dyer G M, Bernstein A C, Cho B I, Osterholz J, Grigsby W, Dalton A, Shepherd R, Ping Y, Chen H, Widmann K and Ditmire T 2008 *Phys. Rev. Lett.* **101**(1) 015002
- [6] Mančić A, Lévy A, Harmand M, Nakatsutsumi M, Antici P, Audebert P, Combis P, Fourmaux S, Mazevet S, Peyrusse O, Recoules V, Renaudin P, Robiche J, Dorchie F and Fuchs J 2010 *Phys. Rev. Lett.* **104**(3) 035002
- [7] Roth M, Jung D, Falk K, Guler N, Deppert O, Devlin M, Favalli A, Fernandez J, Gautier D, Geissel M, Haight R, Hamilton C E, Hegelich B M, Johnson R P, Merrill F, Schaumann G, Schoenberg K, Schollmeier M, Shimada T, Taddeucci T, Tybo J L, Wagner F, Wender S A, Wilde C H and Wurden G A 2013 *Phys. Rev. Lett.* **110**(4) 044802
- [8] Dromey B, Coughlan M, Senje L, Taylor M, Kuschel S, Villagomez-Bernabe B, Stefanuik R, Nersisyan G, Stella L, Kohanoff J *et al.* 2016 *Nat. Commun.* **7** 10642
- [9] Barberio M, Scisciò M, Vallières S, Cardelli F, Chen S, Famulari G, Gangolf T, Revet G, Schiavi A, Senzacqua M *et al.* 2018 *Nat. Commun.* **9** 372
- [10] Higginson D, Korneev P, Ruyer C, Riquier R, Moreno Q, Béard J, Chen S, Grassi A, Grech M, Gremillet L *et al.* 2019 *Commun. Phys.* **2** 1–7
- [11] Bulanov S, Esirkepov T, Khoroshkov V, Kuznetsov A and Pegoraro F 2002 *Physics Letters A* **299** 240 – 247
- [12] Linz U and Alonso J 2007 *Phys. Rev. ST Accel. Beams* **10**(9) 094801
- [13] Denavit J 1992 *Phys. Rev. Lett.* **69** 3052–3055
- [14] Silva L O, Marti M, Davies J R, Fonseca R A, Ren C, Tsung F S and Mori W B 2004 *Phys. Rev. Lett.* **92**(1) 015002
- [15] Romagnani L, Bulanov S V, Borghesi M, Audebert P, Gauthier J C, Löwenbrück K, Mackinnon A J, Patel P, Pretzler G, Toncian T and Willi O 2008 *Phys. Rev. Lett.* **101** 025004
- [16] Haberberger D, Tochitsky S, Fiuza F, Gong C, Fonseca R A, Silva L O, Mori W B and Joshi C 2012 *Nat. Phys.* **8** 95–99
- [17] Fiuza F, Stockem A, Boella E, Fonseca R A, Silva L O, Haberberger D, Tochitsky S, Gong C, Mori W B and Joshi C 2012 *Phys. Rev. Lett.* **109**(21) 215001
- [18] Pak A, Kerr S, Lemos N, Link A, Patel P, Albert F, Divol L, Pollock B B, Haberberger D, Froula D, Gauthier M, Glenzer S H, Longman A, Manzoor L, Fedosejevs R, Tochitsky S, Joshi C and Fiuza F 2018 *Phys. Rev. Accel. Beams* **21** 103401
- [19] Karimabadi H, Roytershteyn V, Vu H X, Omelchenko Y A, Scudder J, Daughton W, Dimmock A, Nykyri K, Wan M, Sibeck D, Tatineni M, Majumdar A, Loring B and Geveci B 2014 *Physics of Plasmas* **21** 062308
- [20] Dieckmann M E, Doria D, Sarri G, Romagnani L, Ahmed H, Folini D, Walder R, Bret A and Borghesi M 2017 *Plasma Physics and Controlled Fusion* **60** 014014
- [21] Perkins L J, Betti R, LaFortune K N and Williams W H 2009 *Phys. Rev. Lett.* **103**(4) 045004
- [22] Bellei C, Rinderknecht H, Zylstra A, Rosenberg M, Sio H, Li C K, Petrasso R, Wilks S C and Amendt P A 2014 *Physics of Plasmas* **21** 056310
- [23] Santos J J, Vauzour B, Touati M, Gremillet L, Feugeas J L, Ceccotti T, Bouillaud R, Deneuille F, Floquet V, Fourment C, Hadj-Bachir M, Hulin S, Morace A, Nicolai P, d’Oliveira P, Reau

- F, Samaké A, Tcherbakoff O, Tikhonchuk V T, Veltcheva M and Batani D 2017 *New Journal of Physics* **19** 103005
- [24] Spitkovsky A 2008 *The Astrophysical Journal* **682** L5–L8
- [25] Lemoine M, Gremillet L, Pelletier G and Vanthieghem A 2019 *Phys. Rev. Lett.* **123**(3) 035101
- [26] Stockem A, Fiuza F, Bret A, Fonseca R and Silva L 2014 *Scientific reports* **4** 3934
- [27] Sundström A, Juno J, TenBarge J M and Pusztai I 2019 *J. Plasma Phys.* **85** 905850108
- [28] Turrell A E, Sherlock M and Rose S J 2015 *Nat. Commun.* **6** 8905
- [29] Sundström A, Siminos E, Gremillet L and Pusztai I 2020 Fast collisional electron heating and relaxation with circularly polarized ultra-intense short-pulse laser *Submitted for publication in J. Plasma Phys. (Preprint <https://arxiv.org/abs/1911.09562>)*
- [30] Derouillat J, Beck A, Pérez F, Vinci T, Chiaramello M, Grassi A, Flé M, Bouchard G, Plotnikov I, Aunai N, Dargent J, Riconda C and Grech M 2018 *Comput. Phys. Commun.* **222** 351
- [31] Pérez F, Gremillet L, Decoster A, Drouin M and Lefebvre E 2012 *Phys. of Plasmas* **19** 083104
- [32] Kruer W L and Estabrook K 1985 *The Phys. of Fluids* **28** 430–432
- [33] Bauer D and Mulser P 2007 *Physics of Plasmas* **14** 023301
- [34] May J, Tonge J, Fiuza F, Fonseca R A, Silva L O, Ren C and Mori W B 2011 *Phys. Rev. E* **84** 025401
- [35] Pusztai I, TenBarge J M, Csapó A N, Juno J, Hakim A, Yi L and Fülöp T 2018 *Plasma Physics and Controlled Fusion* **60** 035004
- [36] Arber T D, Bennett K, Brady C S, Lawrence-Douglas A, Ramsay M G, Sircombe N J, Gillies P, Evans R G, Schmitz H, Bell A R and Ridgers C P 2015 *Plasma Physics and Controlled Fusion* **57** 113001
- [37] Sentoku Y and Kemp A 2008 *J. of Comput. Phys.* **227** 6846–6861
- [38] Nanbu K 1997 *Phys. Rev. E* **55**(4) 4642–4652
- [39] Nanbu K and Yonemura S 1998 *Journal of Computational Physics* **145** 639 – 654 ISSN 0021-9991
- [40] Bhadoria S, Kumar N and Keitel C H 2019 Stable quasi-monoenergetic ion acceleration from the laser-driven shocks in a collisional plasma *Version 2 contains a comparison between two PIC collision algorithms. (Preprint <https://arxiv.org/abs/1707.03309v2>)*